

Scaling silicon photonic switch fabrics for data center interconnection networks

Dessislava Nikolova,^{*} Sébastien Rumley, David Calhoun, Qi Li, Robert Hendry, Payman Samadi, and Keren Bergman

Electrical Engineering Department, Columbia University, 500 West 120th street, New York, NY, 10027, USA
^{*}dnn2108@columbia.edu

Abstract: With the rapidly increasing aggregate bandwidth requirements of data centers there is a growing interest in the insertion of optically interconnected networks with high-radix transparent optical switch fabrics. Silicon photonics is a particularly promising and applicable technology due to its small footprint, CMOS compatibility, high bandwidth density, and the potential for nanosecond scale dynamic connectivity. In this paper we analyze the feasibility of building silicon photonic microring based switch fabrics for data center scale optical interconnection networks. We evaluate the scalability of a microring based switch fabric for WDM signals. Critical parameters including crosstalk, insertion loss and switching speed are analyzed, and their sensitivity with respect to device parameters is examined. We show that optimization of physical layer parameters can reduce crosstalk and increase switch fabric scalability. Our analysis indicates that with current state-of-the-art devices, a high radix 128×128 silicon photonic single chip switch fabric with tolerable power penalty is feasible. The applicability of silicon photonic microrings for data center switching is further supported via review of microring operations and control demonstrations. The challenges and opportunities for this technology platform are discussed.

©2015 Optical Society of America

OCIS codes: (130.4815) Optical switching devices; (130.3120) Integrated optics devices; (200.4650) Optical interconnects; (200.6715) Switching.

References and links

1. N. Farrington, G. Porter, S. Radhakrishnan, H. H. Baz-Zaz, V. Subramanya, Y. Fainman, G. Papen, and A. Vahdat, "Helios: A hybrid electrical/optical switch architecture for modular data centers," in *Proceedings of the ACM SIGCOMM 2010 Conference* (2010).
2. G. Wang, D. G. Andersen, M. Kaminsky, K. Papagian-Naki, T. E. Ng, M. Kozuch, and M. Ryan, "c-through: part-time optics in data centers," in *Proceedings of the ACM SIG COMM 2010 Conference* (2010).
3. Calient S320 optical circuit switching. <http://www.calient.com>.
4. Polatis series 6000. <http://www.polatis.com>.
5. S. Rumley, D. Nikolova, R. Hendry, Q. Li, D. Calhoun, and K. Bergman, "Silicon photonics for exascale systems," *J. Lightwave Technol.* (to be published).
6. M. Lipson, "Guiding, modulating, and emitting light on silicon—challenges and opportunities," *J. Lightwave Technol.* **23**(12), 4222–4238 (2005).
7. R. Hendry, D. Nikolova, S. Rumley, and K. Bergman, "Modeling and evaluation of chip-to-chip scale silicon photonic networks," in *Proceedings of IEEE Symposium on High Performance Interconnects (Hot Interconnects)* (2014).
8. A. Poon, X. Luo, F. Xu, and H. Chen, "Cascaded microresonator-based matrix switch for silicon on-chip optical interconnection," *Proc. IEEE* **97**(7), 1216–1238 (2009).
9. B. G. Lee, A. Biberman, J. Chan, and K. Bergman, "High-performance modulators and switches for silicon photonic networks-on-chip," *IEEE J. Sel. Top. Quantum Electron.* **16**(1), 6–22 (2010).
10. S. Han, T. J. Seok, N. Quack, B. Yoo, and M. C. Wu, "Monolithic 50x50 MEMS silicon photonic switches with microsecond response time," in *Optical Fiber Communication Conference*, (Optical Society of America, 2014), paper M2K.2.

11. K. Suzuki, K. Tanizawa, T. Matsukawa, G. Cong, S.-H. Kim, S. Suda, M. Ohno, T. Chiba, H. Tadokoro, M. Yanagihara, Y. Igarashi, M. Masahara, S. Namiki, and H. Kawashima, "Ultra-compact 8×8 strictly-non-blocking Si-wire PILOSS switch," *Opt. Express* **22**(4), 3887–3894 (2014).
12. P. Dong, S. Liao, H. Liang, R. Shafiiha, D. Feng, G. Li, X. Zheng, A. V. Krishnamoorthy, and M. Asghari, "Submilliwatt, ultrafast and broadband electro-optic silicon switches," *Opt. Express* **18**(24), 25225–25231 (2010).
13. A. V. Rylyakov, C. L. Schow, B. G. Lee, W. M. J. Green, S. Assefa, F. E. Doany, Y. Min, J. Van Campenhout, C. V. Jahnes, J. A. Kash, and Y. A. Vlasov, "Silicon photonic switches hybrid-integrated with CMOS drivers," *IEEE J. Solid-State Circuits* **47**(1), 345–354 (2012).
14. B. G. Lee, A. V. Rylyakov, W. M. J. Green, S. Assefa, C. W. Baks, R. Rimolo-Donadio, D. M. Kuchta, M. H. Khater, T. Barwicz, C. Reinholm, E. Kiewra, S. M. Shank, C. L. Schow, and Y. A. Vlasov, "Monolithic silicon integration of scaled photonic switch fabrics, CMOS logic, and device driver circuits," *J. Lightwave Technol.* **32**(4), 743–751 (2014).
15. Q. Cheng, A. Wonfor, R. V. Penty, and I. White, "Scalable, low-energy hybrid photonic space switch," *J. Lightwave Technol.* **31**(18), 1385–1391 (2013).
16. L. Chen, E. Hall, L. Theogarajan, and J. Bowers, "Photonic switching for data center applications," *IEEE Photon. J.* **3**(5), 834–844 (2011).
17. X. Zhu, Q. Li, J. Chan, A. Ahsan, H. L. R. Lira, M. Lipson, and K. Bergman, "4 44 Gb/s packet-level switching in a second-order microring switch," *IEEE Photon. Technol. Lett.* **24**(17), 1555–1557 (2012).
18. L. Xu, W. Zhang, Q. Li, J. Chan, H. L. R. Lira, M. Lipson, and K. Bergman, "40-Gb/s DPSK data transmission through a silicon microring switch," *IEEE Photon. Technol. Lett.* **24**(6), 473–475 (2012).
19. N. Sherwood-Droz, H. Wang, L. Chen, B. G. Lee, A. Biberman, K. Bergman, and M. Lipson, "Optical 4x4 hitless silicon router for optical networks-on-chip (NoC)," *Opt. Express* **16**(20), 15915–15922 (2008).
20. B. G. Lee, W. M. J. Green, J. V. Campenhout, C. L. Schow, A. V. Rylyakov, S. Assefa, M. Yang, J. Rosenberg, J. A. Kash, and Y. A. Vlasov, "Comparison of ring resonator and Mach-Zehnder photonic switches integrated with digital CMOS drivers," presented at 2010 IEEE Photonic Society's 23rd Annual Meeting, 2010.
21. T. Shiraishi, Q. Li, Y. Liu, X. Zhu, K. Padmaraju, R. Ding, M. Hochberg, and K. Bergman, "A reconfigurable and redundant optically-connected memory system using a silicon photonic switch," in *Optical Fiber Communication Conference* (Optical Society of America, 2014), paper Th2A.10.
22. W. Zhang, L. Xu, Q. Li, H. L. R. Lira, M. Lipson, and K. Bergman, "Broadband silicon photonic packet-switching node for large-scale computing systems," *IEEE Photon. Technol. Lett.* **24**(8), 688–690 (2012).
23. L. Chen, A. Sohdi, J. E. Bowers, L. Theogarajan, J. Roth, and G. Fish, "Electronic and photonic integrated circuits for fast data center optical circuit switches," *IEEE Commun. Mag.* **51**(9), 53–59 (2013).
24. A. Bianco, D. Cuda, R. Gaudino, G. Gavilanes, F. Neri, and M. Petracca, "Scalability of optical interconnects based on microring resonators," *IEEE Photon. Technol. Lett.* **22**(15), 1081–1083 (2010).
25. D. Nikolova, R. Hendry, S. Rumley, and K. Bergman, "Scalability of silicon photonic microring based switch," in *Proceedings of 16th International Conference on Transparent Optical Networks (ICTON)*, (2014).
26. T.-Y. Feng, "A survey of interconnection networks," *IEEE Computer* **14**(12), 12–27 (1981).
27. A. Yariv, "Universal relations for coupling of optical power between microresonators and dielectric waveguides," *Electron. Lett.* **36**(4), 321 (2000).
28. A. Yariv and P. Yeh, *Photonics: Optical Electronics in Modern Communications* (Oxford University Press, 2007).
29. D. Nikolova and K. Bergman, "Analysis of silicon photonic microring-based multistage switches," in *Proceedings of Advanced Photonics for Communications* (Optical Society of America, 2014), paper JT2B.3.
30. B. A. Small, B. G. Lee, and K. Bergman, "On cascades of resonators for high-bandwidth integrated optical interconnection networks," *Opt. Express* **14**(22), 10811–10818 (2006).
31. M. Yang, W. M. Green, S. Assefa, J. Van Campenhout, B. G. Lee, C. V. Jahnes, F. E. Doany, C. L. Schow, J. A. Kash, and Y. A. Vlasov, "Non-blocking 4x4 electro-optic silicon switch for on-chip photonic networks," *Opt. Express* **19**(1), 47–54 (2011).
32. R. Soref and B. Bennett, "Electrooptical effects in silicon," *IEEE J. Quantum Electron.* **23**(1), 123–129 (1987).
33. C. A. Barrios, V. R. Almeida, R. Panepucci, and M. Lipson, "Electrooptic modulation of silicon on insulator submicrometer-size waveguide devices," *J. Lightwave Technol.* **21**(10), 2332–2339 (2003).
34. R. Ramaswami, K. N. Sivarajan, and G. H. Sasaki, *Optical Networks: A Practical Perspective* (Elsevier, 2010).
35. M. Pantouvaki, H. Yu, M. Rakowski, P. Christie, P. Verheyen, G. Lepage, N. Van Hoovels, P. Absil, and J. Van Campenhout, "Comparison of silicon ring modulators with interdigitated and lateral p-n junctions," *IEEE J. Sel. Top. Quantum Phys.* **19**(2), 7900308 (2013).
36. M. Gnan, S. Thoms, D. S. Macintyre, R. M. De La Rue, and M. Sorel, "Fabrication of low-loss photonic wires in silicon-on-insulator using hydrogen silsesquioxane electron-beam resist," *Electron. Lett.* **44**(2), 115–116 (2008).
37. Y. A. Vlasov and S. J. McNab, "Losses in single-mode silicon-on-insulator strip waveguides and bends," *Opt. Express* **12**(8), 1622–1631 (2004).
38. J. Cardenas, C. B. Poitras, J. T. Robinson, K. Preston, L. Chen, and M. Lipson, "Low loss etchless silicon photonic waveguides," *Opt. Express* **17**(6), 4752–4757 (2009).
39. P. Dong, W. Qian, S. Liao, H. Liang, C.-C. Kung, N.-N. Feng, R. Shafiiha, J. Fong, D. Feng, A. V. Krishnamoorthy, and M. Asghari, "Low loss shallow-ridge silicon waveguides," *Opt. Express* **18**(14), 14474–14479 (2010).

40. G. Li, A. Krishnamoorthy, I. Shubin, J. Yao, Y. Luo, H. Thacker, X. Zheng, K. Raj, and J. E. Cunningham, “Ring resonator modulators in silicon for interchip photonic links,” *IEEE J. Sel. Top. Quantum Electron.* **19**(6), 95 (2013).
41. M. Masi, “Modeling of sequences of silicon micro-resonators for on-chip optical routing and switching,” thesis, U. Trento (2011).
42. Q. Xu, D. Fattal, and R. G. Beausoleil, “Silicon microring resonators with 1.5-microm radius,” *Opt. Express* **16**(6), 4309–4315 (2008).
43. Q. Li, D. Calhoun, Y. Liu, R. Ding, T. Baehr-Jones, M. Hochberg, and K. Bergman, “Single microring-based 2×2 silicon photonic crossbar switches for on-chip optical interconnects,” submitted to *Opt. Express*.
44. F. Xia, L. Sekaric, and Y. A. Vlasov, “Mode conversion losses in silicon-on-insulator photonic wire based racetrack resonators,” *Opt. Express* **14**(9), 3872–3886 (2006).
45. W. Dally and B. Towles, *Principles and Practices of Interconnection Networks* (Elsevier, 2004).
46. Y. Ma, Y. Zhang, S. Yang, A. Novack, R. Ding, A. E. Lim, G. Q. Lo, T. Baehr-Jones, and M. Hochberg, “Ultralow loss single layer submicron silicon waveguide crossing for SOI optical interconnect,” *Opt. Express* **21**(24), 29374–29382 (2013).
47. D. Calhoun, K. Wen, X. Zhu, S. Rumley, L. Luo, Y. Liu, R. Ding, T. Baehr-Jones, M. Hochberg, M. Lipson, and K. Bergman, “Dynamic reconfiguration of silicon photonic circuit switched interconnection networks,” in *Proceedings of IEEE High Performance Extreme Computing Conference (HPEC)* (2014).
48. K. Padmaraju, D. F. Logan, X. Zhu, J. J. Ackert, A. P. Knights, and K. Bergman, “Integrated thermal stabilization of a microring modulator,” *Opt. Express* **21**(12), 14342–14350 (2013).
49. K. Padmaraju and K. Bergman, “Resolving the thermal challenges for silicon microring resonator devices,” *Nanophotonics* **3**(4–5), 269–281 (2013).
50. D. Calhoun, Q. Li, C. Browning, N.C. Abrams, Y. Liu, R. Ding, L.P. Barry, T. Baehr-Jones, M. Hochberg, K. Bergman, “Programmable Wavelength Locking and Routing in a Silicon-Photonic Interconnection Network Implementation” submitted to OFC 2015.
51. X. X. Zheng, J. E. Cunningham, G. Li, Y. Luo, H. Thacker, J. Yao, R. Ho, J. Lexau, F. Liu, D. Patil, P. Amberg, N. Pinckney, P. Dong, D. Feng, M. Asghari, A. Mekis, T. Pinguet, K. Raj, and A. V. Krishnamoorthy, “Ultralow power silicon photonic transceivers for inter/intra-chip interconnects,” *Proc. SPIE* **7797**, 779702 (2010).
52. A. Yariv, “Critical coupling and its control in optical waveguide-ring resonator systems,” *IEEE Photon. Technol. Lett.* **14**(4), 483–485 (2002).
53. D. A. B. Miller, “Designing linear optical components,” *Optics in 2013 Special Issue, Optics and Photonics News*, December 2013, p. 38.
54. Y. Long and J. Wang, “Optically-controlled extinction ratio and Q-factor tunable silicon microring resonators based on optical forces,” *Sci. Rep.* **4**, 5409 (2014).
55. V. M. Menon, W. Tong, and S. R. Forrest, “Control of quality factor and critical coupling in microring resonators through integration of a semiconductor optical amplifier,” *IEEE Photon. Technol. Lett.* **16**(5), 1343–1345 (2004).
56. Y. Qian, H. Mehrvar, H. Ma, X. Yang, K. Zhu, H. Y. Fu, D. Geng, D. Goodwill, P. Dumais, and E. Bernier, “Crosstalk optimization in low extinction-ratio switch fabrics,” in *Optical Fiber Communication Conference*, **Vol. 2** of 2014, paper Th11.4.
57. A. Biberman, G. Hendry, J. Chan, H. Wang, K. Bergman, K. Preston, N. Sherwood-Droz, J. S. Levy, and M. Lipson, “CMOS-compatible scalable photonic switch architecture using 3D-integrated deposited silicon materials for high-performance data center networks,” in *Optical Fiber Communication Conference* (Optical Society of America, 2011) paper OMM2.
58. N. Sherwood-Droz and M. Lipson, “Scalable 3D dense integration of photonics on bulk silicon,” *Opt. Express* **19**(18), 17758–17765 (2011).
59. A. Gondarenko, J. S. Levy, and M. Lipson, “High confinement micron-scale silicon nitride high Q ring resonator,” *Opt. Express* **17**(14), 11366–11370 (2009).

1. Introduction

The continuous growth in cloud-based applications and big data analytics has drastically changed the scale of data center networks. Current high performance data centers consist of hundreds of thousands of servers, which require a large and efficient interconnection network. The main challenge is providing a fast and non-blocking switching platform that is low cost, energy efficient and supports large-scale topologies. In conventional intra-data center networks, electronic packet switching is used as the switching substrate. Conventional electronic switching and interconnection network platforms operate with significant power consumption that grows with data rates and moreover are designed to work at only a specific data rate. Increased bandwidth demands and power consumption limitations related to scalability of the switching substrate call for an increased use of optics in data centers. Optical wavelength division multiplexing (WDM) provides terabit data transmission and optical

switching can fundamentally provide fast and low energy switching functionalities for intra-data center networks.

Optical point-to-point (P2P) links are extensively used in current data centers for rack-to-rack connectivity. However utilizing optical links for P2P data transmission requires optical-to-electrical (O/E) and electrical-to-optical (E/O) conversions at each rack as switching is still performed in the electrical domain. Hybrid architectures have been proposed that simultaneously interconnect racks with optical circuit switching and electrical packet switching [1, 2], providing the optical switching fabric by a 3D micro-electro-mechanical systems (MEMS) or piezoelectric free-space switch [3, 4]. Introduction of optical switching in data centers would make an immediate improvement in energy efficiency since it eliminates the O/E/O conversions at the switches. However, while these switches are commercially available with several hundred ports, their inherent millisecond switching times makes them efficient only for large and steady flows. A large-scale integrated optical switching substrate with nanosecond switching speed and low energy consumption would address a larger fraction of the intra- data center traffic delivering substantial performance gains.

Silicon photonics [5, 6] is an excellent candidate technology for realizing such ultra-high-speed optical switches. It provides small area footprint, low power consumption (due to the close proximity of electronic drivers) and the potential for reduced fabrication costs at large scales. Silicon photonic switches have received significant research interest in the past several years for realizing intra-chip and intra-node interconnects [7–9] as well as inter-node interconnects for data centers or supercomputers. Integrated optical switching can be performed with various device configurations including, Mach-Zehnder (MZ) interferometers, 2D MEMS, and microrings. A recent demonstration of a monolithic 2D MEMS silicon photonic switch has shown a 50×50 port count with 2500 switching elements and microsecond response time [10]. A drawback of MEMS-based switches is that they typically require large driving voltages and thus have high power consumption. An 8×8 strictly non-blocking switch matrix consisting of 64 integrated MZ elements and switching of 43 Gb/s QPSK signals has also been reported [11]. However, this matrix is based on thermo optic effect, which is expected to have approximately microsecond response time.

Since faster switching speeds approaching packet transmission rates are desirable in data center applications, both academic and industry research efforts have investigated nanosecond-scale switching architectures based primarily on MZ and microring switching elements. Nanosecond-scale operation is made possible by exploiting electro-optic effects, as opposed to thermo-optic effects. Oracle has demonstrated a 2×2 electro-optic MZ switch with 6 ns switching time and 0.6 mW switching power [12]. IBM has shown both hybrid [13] and monolithic [14] integration of silicon photonic switches with complementary metal oxide semiconductors (CMOS) drivers in 2×2 , 4×4 , and 8×8 configurations. The switch fabric characterization indicates that a majority of the static power consumption is due to the phase tuners of the MZ switches [14]. To compensate for cascaded insertion losses of switching elements and further scale the photonic switch, hybrid approaches [15, 16] that integrate silicon MZ switches and III-V materials for semiconductor optical amplifiers (SOA) have been proposed. Integrating SOAs allows the overall insertion loss of the chip to be zero; however, SOAs consume additional power with a typically poor energy efficiency profile.

Microring based switch fabrics have been shown to support WDM switching [17] for a diversity of high speed modulation formats [18] and in non-blocking configurations [19]. A recent comparison of microring and MZ switches integrated with CMOS drivers [20] has shown the advantage of microring over MZ switches in terms of power consumption. System-level demonstrations have shown broadband packet-level switching, where either MZ [21] or microring [22] based switches are used to connect field programmable gate arrays (FPGA)-emulated systems such as CPU and memory nodes. A custom CMOS integrated circuit was designed and tightly integrated with a photonic switch fabric [23] in order to control the switch. These demonstrations pave the way towards larger switch fabric experiments where

optical network interfaces interconnect the photonic substrate and enable the investigation of realistic data center applications.

In this work we analyze the scalability of a silicon photonic switch fabric composed of 2×2 switch elements. Each of the switch elements consists of two microrings at the intersection of two waveguides. We develop a detailed model to evaluate the insertion loss and crosstalk of the switching fabric. While prior studies [24] have examined these issues, they were based on simplified models, which did not take into account physical layer parameters. In [25] the scalability of the switch fabric was estimated without accounting for the critical waveguide crossings. The model described in this paper provides a complete physical layer model for the crosstalk and insertion losses arising from the 2×2 switching elements and is scaled to evaluate switch fabric planar architectures. We propose an approximation for the loss and crosstalk arising from the crossings typically present in these architectures. Our modeling approach allows us to analyze in detail the behavior of the resulting optical switch fabric, and to identify the critical device parameters and their optimal values. Furthermore we address the challenges of integrating the silicon photonic switching fabric in a larger system and demonstrate its applicability to optically interconnected data centers.

In the next section we describe the microring switch transmission characteristics and basic operation. We calculate the expected crosstalk and insertion loss and analyze its suitability for WDM switching operation. In Section 3 our modeling approach is applied to evaluate the scalability of a switching fabric composed from these switching elements. The current approaches to system level integration, control and management are reviewed in Section 4. These demonstrate the feasibility of integrated system solutions for silicon photonic microring switching fabrics. Section 5 discusses the advances necessary to achieve scalable energy efficient microring based switch fabrics. Section 6 concludes the article.

2. Silicon photonic microrings based 2×2 switch

2.1 Transmission characteristics and basic operation

The basic 2×2 switching element, schematically drawn in Fig. 1, consists of two silicon microring resonators and two crossing silicon waveguides. When the rings are ON resonance with an input signal, this signal is coupled to the ring, then coupled back to the second waveguide. In this way, the signal is “dropped” onto the other waveguide as shown in Fig. 1(a). When the rings are OFF resonance, the signal passes through the switching element remaining on the same waveguide as shown in Fig. 1(b). Both input signals can be dropped into or allowed to pass by the rings simultaneously which allows this type of switch to be used as a full 2×2 switching element for composing more complex switch architectures [26].

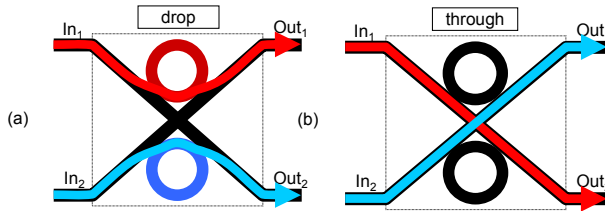


Fig. 1. 2×2 Switching element in (a) “drop” and (b) “through” state.

In order to relate the output signal powers P_{out1}, P_{out2} to the input power P_{in} we model the switch using the transfer matrix method [27, 28]. The 2×2 switch in question is a coupled system with transfer matrices as described in [29]. The transmission of the switch depends on the parameters as grouped in Table 1, which will be used throughout the text:

Table 1. Parameters for switch transmission description

Parameter	Description
t_1, t_2	field transmission coefficients of the couplers (referred also as coupling coefficients throughout the text)
l_r	round trip field loss in the ring $l_r = e^{-\alpha L/2}$
l_{wg}	field loss in the waveguide connecting the two rings $l_{wg} = e^{-\alpha_{wg} L_{wg}/2}$
α_{wg}	optical power absorption coefficient of the waveguides
L_{wg}	travel distance of optical mode between the two rings
L	round trip travel distance of optical mode in the ring
ϕ	round trip phase of the ring $\phi = (2\pi/\lambda) n_{eff} L$
α	optical power absorption coefficient of the ring waveguide
n_{eff}	effective refractive index
Δn_{eff}	$-(8.8 \times 10^{-22} dN + 8.5 \times 10^{-18} dP^{0.8})$ effective refractive index change due to change in the carriers concentration
$\Delta \alpha$	$8.5 \times 10^{-18} dN + 6 \times 10^{-18} dP$ the absorption coefficient index change due to change in the carriers concentration
dN (dP)	electron (hole) concentration change in cm^{-3}

The rings are on resonance with an input signal when round trip phase of the ring $\phi = 0$. When on resonance and provided that $t_1 = l_r t_2$, the ratio between the input and output power through the switch is

$$\frac{P_{out1}}{P_{in1}}(\phi = 0) = D = \frac{l_r^{1/2}(1-t_2^2)}{1-l_r^2 t_2^2} \quad (1)$$

When the rings are off resonance with the round trip phase $\phi = \pi$, the ratio between the input and output powers is found to be given with

$$\frac{P_{out2}}{P_{in1}}(\phi = \pi) = T = \frac{l_{wg}^4 (l_r t_1 + t_2)^2 (t_1 + l_r t_2)^2 t_c^4}{(1+l_r t_1 t_2)^4 + l_r^3 l_{wg}^4 (1-t_1^2)^2 (1-t_2^2)^2 t_c^4} \quad (2)$$

Part of the input signal P_{in1} couples through the ring giving rise to crosstalk

$$\frac{P_{out1}}{P_{in1}}(\phi = \pi) = T_x = \frac{l_r^{1/2}(1-t_1^2)^2(1-t_2^2)^2(1+l_r t_1 t_2)^2(1+l_r l_{wg}^4 t_c^4)}{(1+l_r t_1 t_2)^4 + l_r^3 l_{wg}^4 (1-t_1^2)^2 (1-t_2^2)^2 t_c^4} \quad (3)$$

The transmission through the switching element is shown in Fig. 2. The dashed curve shows the transmission on *Out2* when there is only a signal on *In1*, i.e. P_{out2} / P_{in1} . The full curve shows the transmission on *Out1*, i.e. P_{out1} / P_{in1} . Resonances in the transmission spectrum are determined according to the refractive index and the size of the ring by $\lambda_m = n_{eff,m} L$.

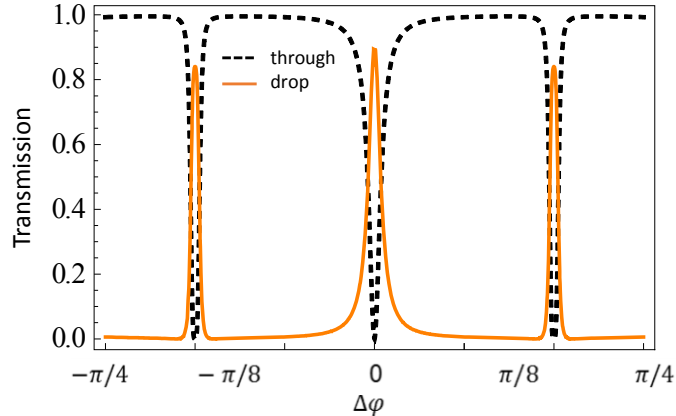


Fig. 2. Transmission through the switch versus the round trip phase of the ring $\varphi = (2\pi/\lambda) n_{\text{eff}}$ on the “through” (dashed line) and “drop” port (full line).

The switching element resonances are of second order exhibiting alternating Butterworth type (i.e. maximally flat) and type I Chebyshev filters responses [30]. Figure 3 shows the different resonant shapes versus the detuning from the resonance in comparison with the response of a single ring. While the Butterworth type of resonance is flatter, the Chebyshev type is significantly broader than the response of a Lorentzian type filter exhibited by a single ring with the same parameters. The broader shape of the resonances makes them more attractive for data transmission as higher data rates will be less penalized in comparison with the penalty for Lorentzian type filter. It is worth noting that the geometry of a 2×2 switch can be slightly adapted such that the two waveguides coupling to a ring are parallel. In such a construction the light will traverse half of the ring (instead of one forth as in the considered topology), all the resonance have the same Chebyshev type filter shape.

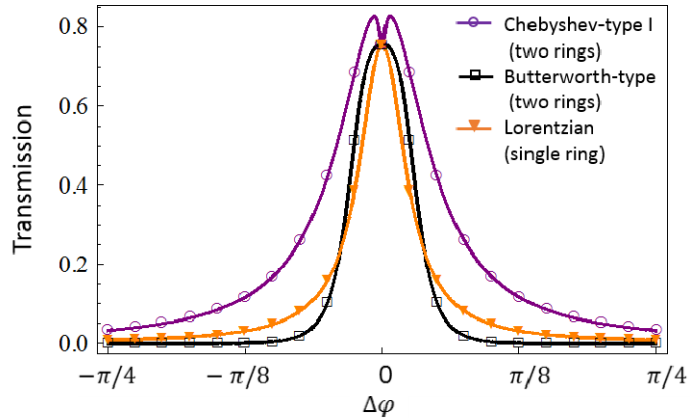


Fig. 3. Transmission at the resonances through a two rings switching element versus the detuning compared with the resonance response of a single microring.

By controlling the rings’ refractive index, using thermal or charge carrier effects in silicon, the state of the 2×2 switch can be manipulated. The operation of an optically controlled switch with the considered geometry has been demonstrated in [31]. Due to the relatively slow response of the thermo-optical effect (order of microseconds), charge carrier based control is generally favored (for a nanosecond order). When microring switching is realized using a p-i-n junction, the application of an electrical signal allows the injection of carriers into the ring. The change in carrier concentration (electrons dN or holes dP) alters the refractive index with Δn_{eff} [32, 33], and hence changes the rings’ resonant frequencies. Carrier

injection affects not only the refractive index but also the loss in the ring with $\alpha' = \alpha + \Delta\alpha$. Both rings have to be controlled simultaneously as the switch needs only two states: a “drop” state—when both rings are on resonance with the wavelength of the signal—and “through” state when both rings are shifted off resonance.

2.2 Crosstalk and loss

When the field transfer coefficient of one of the waveguides matches the total loss in the ring including the transfer coefficient of the other waveguide—i.e. $t_1 = l_r t_2$ —all the signal is coupled from the waveguide to the ring (“dropped”). This is observed in Fig. 2, where at the resonances the transmission on the waveguide drops to 0. This condition is known as critical coupling. If this condition is not realized the power not coupled into the ring will propagate further on the waveguide giving rise to crosstalk. In the considered switch it is sufficient that only one of the coupling regions is realized at the critical coupling—i.e., either $t_1 = l_r t_2$ or $t_2 = l_r t_1$. In this case, even if manufacturing imprecision yields a mismatch between the actual field transmission coefficients and their desired values, one can vary the loss to still achieve critical coupling. The broader resonance shape of the two ring switching element is also beneficial for modulated data because the frequency dependence of the resonance around critical coupling is smaller.

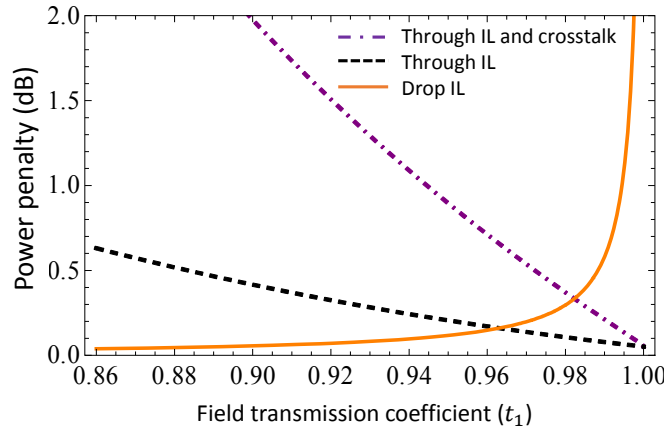


Fig. 4. Power penalty versus the field transmission coefficient t_1 at critical coupling for insertion loss (IL) of a switch in drop through state and crosstalk.

A switching element in through state with incoming signal with power P_2 propagating towards *Out2* will see part of it $P_x = T_x P_2$ couple into the rings and drop onto the waveguide in the undesired direction (*Out1*) giving rise to intra-channel crosstalk. Such crosstalk can interfere constructively or destructively with a signal with power P_1 propagating towards *Out1*. In the case of destructive interference, the power penalty for this signal is given with $PP = -10\log_{10}(1 - 2\sqrt{P_x/P_1})$ [34], and it depends on the signal power of the interfering channel through P_x . The power penalty’s dependence on the field transmission coefficient t_1 at critical coupling is shown in Fig. 4 for equal input power signals $P_1 = P_2$. In the drop state—i.e. $\varphi = 0$ —the signal is almost entirely “dropped” through the ring when t_1 is small, while it is almost entirely attenuated when $t_1 \rightarrow 1$. In through state, $\varphi = \pi$, the transmission dependence is completely the opposite. The sum of transmissions in through and drop state equals 1 in the ideal case where there are no coupling losses. The presence of crosstalk when there are simultaneously two signals on the two inputs significantly changes the power

penalty in through state. As seen from Fig. 4 the strength of the coupling determines to a large extent the switch power penalty. For values of t_1 close to 1 it is very sensitive and small variations in the coupling can have significant impact on the switch transmission. We can immediately see that there is an optimal coupling parameter $t_{1,opt}$ for which the worst case decrease in quality is the same for both switch states $PP_{drop} = PP_{through}$, which is the point where the dot-dashed line crosses the full one in Fig. 4. It is also clear that small deviations in the coupling coefficient result in significant changes in the worst case power penalty. Note that the selection of the optimal coupling parameter as described would result in equal crosstalk power penalties. The output power is dependent on the switch state and on the presence of signals on both inputs.

Figure 5 shows the power penalty versus the absorption coefficient in the ring for $t_1 = 0.96$. Interestingly, the crosstalk is most affected by the loss coefficient. This is indicated by Eq. (3) which shows that the crosstalk is proportional to the square root of the loss in the ring. The transmission spectrum is not symmetric between resonances due to different resonance profiles. This can be exploited by selecting working region centered on resonances with flatter response, resulting in smaller crosstalk. Furthermore the power penalty for a modulated signal has been shown to be the least for such type of filters [30] and moreover less electrical power will be required to shift the resonance as $\Delta\phi \sim \Delta V$ [35].

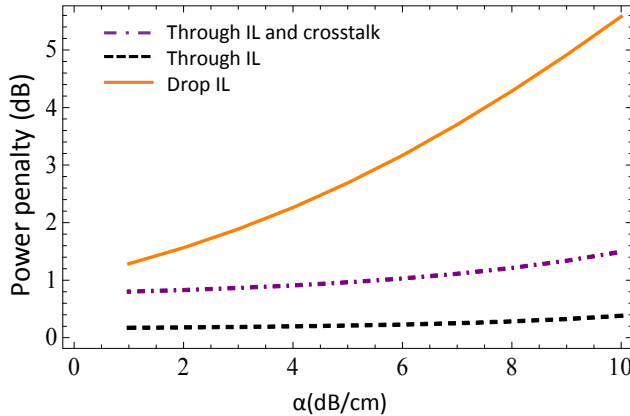


Fig. 5. Power penalty versus the ring absorption coefficient for insertion loss (IL) of a switch in drop and through state, and including the through state crosstalk.

Significantly lower power penalty can be achieved provided the attenuation loss is lower. These losses in the waveguides are heavily affected by geometry and surface roughness. Waveguides with dimensions of approximately 200-250 nm thickness and 450-500 nm width are suitable for compact structures such as microrings due to low bending losses. The lowest propagation for these waveguides is 1-2 dB loss [36, 37]. Note that waveguides with extremely low losses of around 0.3 dB/cm have been reported but with a fabrication process (selective oxidation) that prevent fine dimension controlling [38]. Other waveguide structure like the one reported in [39] are wider and unsuitable for microrings as they have significant bending losses. While we can assume a loss of 1 dB or less for straight waveguides in the switch, state of the art microrings are above this mark.

2.3 Broadband operation

Entire wavelength division multiplexed (WDM) signals can be switched by a single ring in a comb fashion. The broadband characteristics of the switch (i.e. the periodicity of its resonances) are determined from its material and geometrical parameters, namely the ring

size, its group and effective refractive index [40]. These parameters in fact determine the whole set of optical frequencies which will be simultaneously switched by the rings. The free spectral range $FSR = \frac{\lambda^2}{n_g L}$, where n_g is the group index in the ring determines the number of resonances in the spectral range between 1.53 and $1.58 \mu m$ i.e. how many wavelengths a ring can switch simultaneously. Assuming effective refractive index of $n_{eff} = 2.27$ and group index of $n_g = 4.26$ for $\lambda = 1.55 \mu m$ [41] the minimum radius for a ring having a single resonance in the considered $0.05 \mu m$ spectral range ring is $1.8 \mu m$. This dimension is completely in reach of the current manufacturing technologies. Microrings with bending radii of $1.5 \mu m$ and very low bending loss have already been demonstrated [42]. The number of wavelengths N that a ring can switch simultaneously (i.e. has N resonances in the working range) determines the minimum radius for the ring. For example, for the considered parameters it should be $R \geq N 1.8 \mu m$. Larger rings will have higher optical loss lr as the optical path L is longer.

Note that increase in radius does not necessarily result in increased footprint, especially for larger switches as the resonator can take any shape.

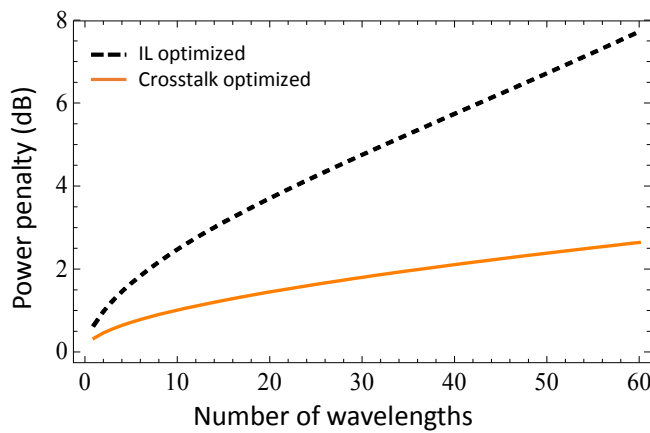


Fig. 6. Power penalty versus the number of wavelengths supported by a switch element in the 50 nm spectrum around $1.55 \mu m$. The field transmission coefficient is optimized for minimizing the power penalty incurred from the insertion losses (IL) and crosstalk.

The optimal coupling coefficient, as shown above, depends on the loss and is therefore different for each ring size that corresponds to a number of wavelengths N . Figure 6 shows the worst case power penalty (i.e. when the crosstalk is maximally destructive) of a switching element supporting different number of wavelengths. In one case the value of the coupling is determined from the condition that the transmission in drop state should equal the transmission in through state. In the second case, the field transmission coefficient at the optimal value is at the point when the power penalty for transmission in drop state equals the worst case power penalty for transmission in through state, accounting for potential crosstalk. It is clear from these results that more wavelengths, and therefore larger rings, will lead to increased power penalties. It is also apparent that a careful optimization of the field transmission coefficient to mitigate both attenuations and crosstalk contributions can provide reduced power penalties. Finally, it is worth noting that a larger ring (corresponding to larger N) results in higher attenuation and reduces the crosstalk contribution to the power penalty. As a result, the optimized field transmission coefficient value (shown in Fig. 7.) decreases with N . The field transmission coefficient depends in general on the wavelength of the signal and the refractive index of the medium, meaning that the optimal value for one wavelength might not be the same for another. These dispersion effects have not been taken into account

in the presented results but should be considered through detailed field simulations for an actual implementation of the switch. Experiments and analysis [43, 44] have shown that a coupler geometry with small dependence of the transmission coefficient on the wavelength across the considered 50nm spectrum is possible. The dispersion effects imply that the methodology reported here returns a slightly underestimated power penalty. For small microrings where the field loss l_i is close to 1 the wavelength dependence is smaller and the approximation is closer to real world scenarios. The estimation of the extra power penalty contribution of this effect and the optimization of the field transmission coefficient across all channels will be addressed in future work.

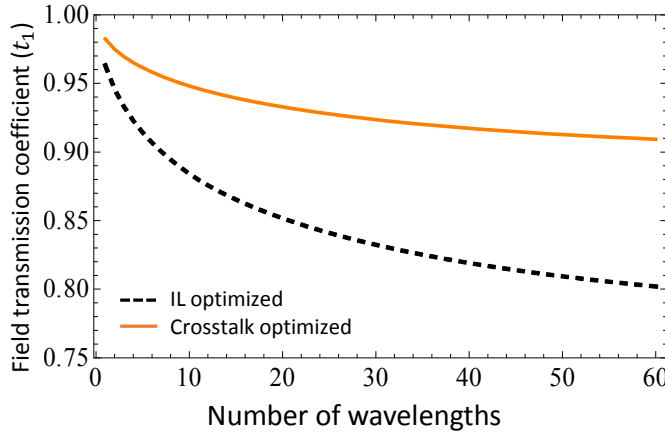


Fig. 7. The field transmission coefficient optimized for insertion loss (IL) and for crosstalk at critical coupling.

The inter-channel crosstalk in a single 2×2 ring switch has been demonstrated to be very low [43] and for the proposed two-ring switch is presumed to be negligible in the considered operational range.

3. Building high radix switch fabrics

3.1 Physical layer scaling

In order to create higher radix switching fabrics, multiple 2×2 switching elements can be interconnected in stages. To form a reconfigurable non-blocking switching fabric we consider the basic switching elements interconnected in Benes network [45]. Consequently a switching fabric with N input and N output ports has $\log_2 N - 1$ stages each consisting of $N/2$ switches as shown on Fig. 8. The interconnection of these $N \log_2 N - N/2$ switching elements translates into waveguide crossings, provided that all waveguides located on the same chip share the same plane. A particular attention must be paid to these crossings, as they both attenuate and generate crosstalk. The maximal number of waveguide crossings traversed by a signal between the stages, as illustrated with the radix 8 topology on Fig. 8, is $N/2 - 1$ crossings after the first stage, $N/4 - 1$ after the second and their number declines until it reaches a single crossing, after which it increases again to reach $N/2 - 1$ before the last stage for a total of $2(N - \log_2 N - 1)$ crossings. For a 32 port switch, the number of crossings is for instance 52. For an 8 ports switch, as visible on Fig. 8, signal traverses up to 8 crossings.

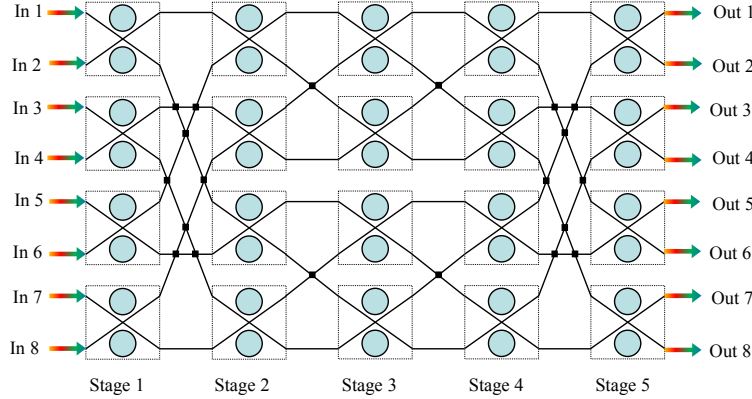


Fig. 8. 8-by-8 multistage switch with Benes topology.

We apply the following recursive procedure in order to evaluate how the crosstalk accumulates across the crossings that separate two stages. Let $P_{S-1,out}^i$ denote the power of the i -th signal incoming from stage S-1. $P_{S-1,out}^{max}$ denotes the maximal signal power that can be forwarded by switching stage S-1 and is given with Eq. (6) explained in detail further in the text. We assume that at each crossing, a maximal power $P_{S-1}^{crossing} = 10^{X/10} P_{S-1,out}^{max}$ can “leak” and perturb $P_{(S-1,out)}^i$, where X is the crosstalk level of a waveguide crossing. Thus, the maximal amount of crosstalk that a signal can receive from N_S crossings is $N_S P_{S-1}^{crossing}$. A schematic representation of this crossings induced crosstalk model is drawn in Fig. 9. This model makes the approximation that all crossings interfere simultaneously and we neglect the interference between the crosstalk signals from the different crossings. We assume that at each crossing, the signal is perturbed by the worst case signal power at this stage. This leads to a slight overestimation of the crosstalk power, since in practice the signal reaching its i -th crossing always encounters a signal that has gone through i crossings, too. These approximations permits to maintain the calculation tractable as we do not have to keep track of the signal at each crossing.

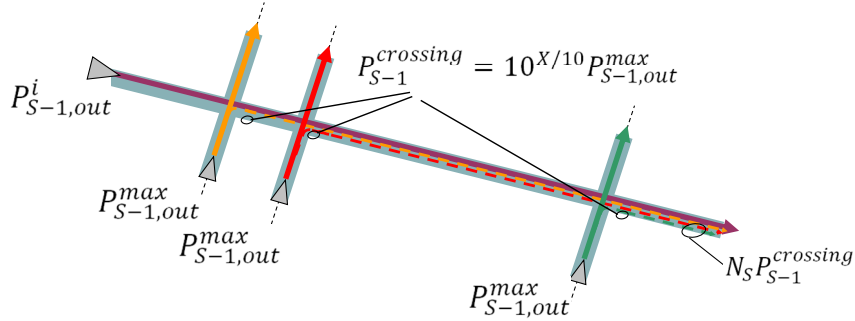


Fig. 9. Schematic representation of the crossings crosstalk model.

Each crossing has an insertion loss \widehat{IL} and the signal is attenuated in the waveguide with l_{wg} before each crossing. The maximum signal at the input of the switch at stage S is therefore

$$P_{S,in}^{max} = IL^{N_c} (P_{S-1,out}^{max} + 2\sqrt{P_{S-1,out}^{max} N_S P_{S-1}^{crossing}} + N_S P_{S-1}^{crossing}), \quad (4)$$

where $IL = l_{wg} \cdot \widehat{IL}$. Applying the same reasoning and approximations the minimum power at the input of stage S is

$$P_{S,in}^{min} = IL^{N_c} (P_{S-1,out}^{min} - 2\sqrt{P_{S-1,in}^{min} N_S P_{S-1}^{crossing}} + N_S P_{S-1}^{crossing}). \quad (5)$$

We now analyze how the minimum and maximum power signals are affected by the switching elements themselves. As discussed in Section 2 at each stage the optimal coupling which minimizes the worst case power penalty is the one for which the power penalties in drop and through state accounting for the crosstalk are equal. As the signal propagates through the switch fabric it accumulates crosstalk not only from the crossings but also from the switching elements. It is exacerbated when at a given stage the interfering signals have higher power than the desired signal. So in order to determine the optimal coupling at each stage, one needs to keep track of both the minimum and maximum accumulated power levels. $P_{S,out}^{min}$ is the minimum output power when the switch is in through state given by $P_{S,out}^{min} = (P_{S,in}^{min} - P_{S,in}^{max})$, given with Eq. (4), is the worst case attenuated signal, which has interfered destructively at the S-1 previous stages. The crosstalk power $P_{S_x} = T_x P_{S,in}^{max}$, where $P_{S,in}^{max}$ given with Eq. (5) and T_x is the crosstalk coefficient from Eq. (3). The optimal coupling for stage S is found from the condition $PP_{drop} = PP_{through}$, hence it is $P_{S,out}^{drop}$ (output power when the switch is in drop state) which gives the minimum power after stage S. Finally the maximum output power from a switch in stage S in through state is obtained when on both inputs the signal powers are at the maximum attainable level for this stage due to constructive interference at the S-1 previous stages i.e.

$$P_{S,out}^{max} = (P_{S,in}^{max} + 2\sqrt{P_{S,in}^{max} P_{S_x}} + P_{S_x}). \quad (6)$$

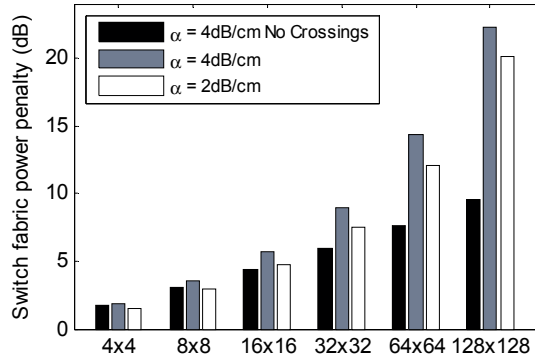


Fig. 10. Switch fabric power penalty versus the switch radix (4 wavelengths).

The power penalty at optimal coupling coefficient versus the radix of a switching fabric dimensioned to switch 4 wavelengths is shown on Fig. 10. The necessary shift in the refractive index Δn_{eff} to operate the switch in through state was calculated for $\varphi = \pi$, which determines the carrier concentration. From it the shift in the absorption coefficient $\Delta\alpha$ is obtained, which determines the loss in the ring due to the change in the carriers concentration in through state. The values for the crossing insertion loss and crosstalk are taken from a recent study [46] which showed 10 μm footprint crossings with $IL_{dB} = -0.028\text{dB}$ insertion loss and $X = -37\text{dB}$ crosstalk. Similar values for the crossing crosstalk have been reported in [16]. The rings were simulated with $\alpha = 4 \text{ dB/cm}$, $\alpha_{wg} = 1 \text{ dB/cm}$, the length L depends on the number of wavelengths. The length of each waveguide in the crossing region is 20 μm . As

was shown on Fig. 5 having a ring with lower loss will reduce the crosstalk. To see this effect for a multistage switch we have simulated the switch fabric also with $\alpha = 2 \text{ dB/cm}$. Reducing the loss of the ring waveguide reduces the crosstalk power penalty and slightly increases the switch scalability. However, as the figure demonstrates the crossings are the main limiting factor to the switch scaling. This is due to the different signal powers that can reach each crossing.

3.2 System level scaling

The power penalty of a switching fabric calculated in the previous section defines the number of wavelengths that can be routed through it within a given optical power budget. Each channel suffers the same (assuming negligible dispersion effects) loss and is penalized by the same impairments. The optical power budget for a WDM system is defined as $P_{\text{Budget}}^{\text{dB}} \geq P_{\text{Loss}}^{\text{dB}} + 10 \log_{10}(N_{\lambda})$. In a full chip-integrated switching fabric context, $P_{\text{Loss}}^{\text{dB}}$ should account not only for the power penalty arising from crosstalk and loss but a penalty for in- and out-coupling the optical signal must be included. In this study we consider 3dB loss per coupler. Due to the presence of non-linear effects in silicon waveguides, the power of signals traveling through the switch fabric must stay below 20dBm. On the other hand, signal powers $> -15 \text{ dBm}$ per channel are typically required at the transmission link end (before the WDM demultiplexing stage) to ensure signal recovery from detector with -20 dBm detector sensitivity [7]. In a scenario where no optical amplification is leveraged, the resulting 35 dB power budget limits the radix of the switching fabric to 128×128 and 6 wavelengths per port. The achievable per port and total number of wavelengths versus the switch radix is shown on Fig. 11 considering microrings with loss $\alpha = 2 \text{ dB/cm}$. Increasing the switch radix means more rings the signal has to traverse and hence higher penalty. However, using rings supporting lower number of wavelengths results in lower power penalty per switching element, as seen on Fig. 5, hence the reduction in the number of per port wavelengths that can be supported for higher switch radix. The total number of wavelengths, obtained by multiplying the per port number with the switch radix, increases. The tuning and trimming power for all the rings for a 128 radix switch fabric, assuming 3.5mW [7] per ring would amount to $\sim 6 \text{ W}$ for a total of 768 wavelengths.

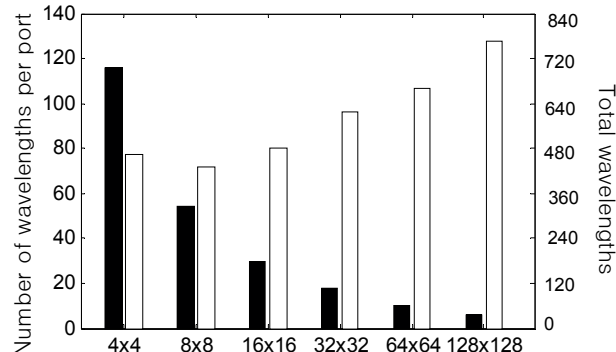


Fig. 11. Number of wavelengths per port (filled bars) and the total wavelengths (empty bars) supported by a switch fabric versus its radix.

The physical and system layer analysis of the switch fabric is necessary to ensure proper functioning of the devices, but not sufficient for a practical integration. In order to integrate silicon photonics based switches in future data center networks, a synchronized control of the various switching elements must be implemented, including development of mechanisms capable of quickly re-establishing a quasi-error-free transmission after a spatial reorganization

of the fabric. In the following section, we provide an overview of the necessary control mechanisms and present an integrated system architecture.

4. Silicon photonic switch fabrics control and data center integration

Integrating nanophotonic switch fabrics in network switches requires implementing mechanisms for arbitration, actuation control and in the case of microrings, thermal stabilization. Simple generation of actuation control signals for MZI-based switch fabrics has been demonstrated using high-speed digital logic implemented in field programmable gate arrays (FPGAs) [21, 47]. Mechanisms for thermal stabilization using control systems have been developed and demonstrated [48, 49]. Control signals can be generated in reaction to some monitoring of the individual element. Ongoing research efforts aim at generating microring control signals using FPGAs coupled to high-speed analog-to-digital (ADC) and digital-to-analog (DAC) devices, based on generation of errors signals [50]. In more advanced prototypes, FPGAs can be replaced by application-specific integrated circuits (ASICs). This will allow further decreasing of the energy footprint of required electrical arbitration logic. Additionally, it has been shown that optimized photonic circuits can be designed such that their fundamental operating states can be switched with an inverter, providing a low-power system solution [51].

The overall mechanism for silicon photonic switch fabric control consists of establishing a switch arbitration plan, according to which actuation signals will be generated. If this plan is locally defined, a switch controller exchanging control messages with (or simply receiving from) the optical network clients must be developed. A protocol through which network clients announce their communication needs and are informed of the optical network availabilities also must be defined. Alternatively, network-wide arbitration can be realized by an independent component, potentially in charge of multiple switch fabrics. In this case, switch fabrics as described in this work simply receive the actuation information corresponding to the near future.

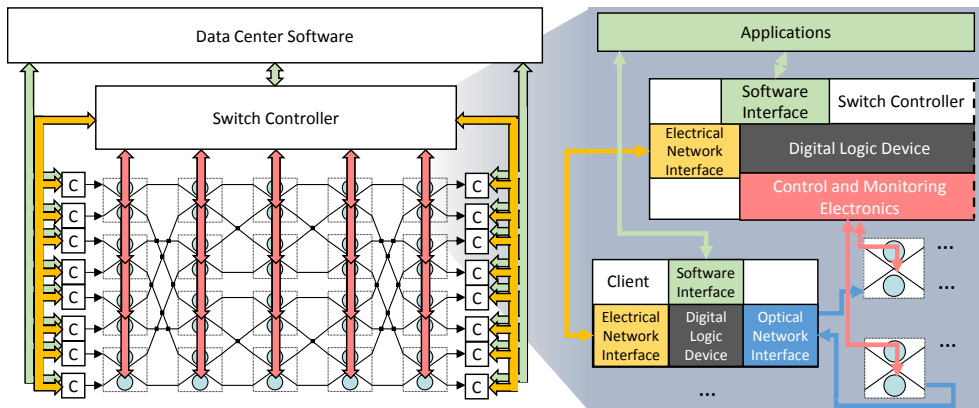


Fig. 12. Silicon photonic computing architecture applicable to data centers, consisting of devices, network control and message passing, and application interfaces.

A combined broadband switching and data center oriented control architecture is depicted in Fig. 12. It shows how a silicon photonic switch receives its commands and can be controlled via an electrical network interface connected to *digital logic devices*. Using the appropriate electrical driving mechanisms for the optics, these devices achieve the system-level configuration. The *electrical network interface* typically receives instructions and commands from the currently deployed *data center software* application. Such an architectural approach is necessary for implementing high-radix silicon photonic microring switching devices in data center interconnection networks.

5. Challenges and opportunities

Our results confirm that silicon photonics microring based switching fabrics have the potential to provide low-cost, energy efficient solutions for future data centers. However, to realize scalable, single chip switching fabrics without integration of SOA between the stages, several challenges need to be addressed.

Designing a coupling region between the ring and the waveguide with precise and possibly adjustable coupling parameters is beneficial for reducing crosstalk. A method to realize this has been proposed and realized [37, 52], where the coupling region is realized as a Mach Zehnder interferometer, allowing for precise setting of the coupling strength. Such an implementation allows also for dynamic control, which can be explored in the future to find the optimal coupling and lowest crosstalk without algorithmic approximations but using the procedure proposed in [53]. Having adjustable coupling would allow each switching element to be optimized for lower power penalty in function of the whole system, for example depending on the nature of the noise in the system. In [54] tunable coupling of a microring switch was demonstrated by realizing one of the waveguides as deformable nanostring. The tuning mechanism relies on the optical force induced deflection of the suspended nanostring. Another method to control the critical coupling is through integration with optical amplifiers [55].

In this study we derived the number of stages in the switching fabric from the desired radix considering a reconfigurable non-blocking Benes interconnection network. Reducing the number of stages will introduce some blocking but will increase the scalability. This has the potential to further allow the increase in throughput and radix with possibly only small penalty in the switching latency. Analysis of the trade-offs of this solution and developing fast optimal scheduling algorithms will be the focus of future work. Another route to increase the scalability is implementing routing algorithms through the switch fabric which optimize the crosstalk [56].

Increasing the switch radix increases the amount and effect of the crossings. In this work we have considered fixed values for the loss and crosstalk which are state-of-the-art for this technology. Designing crossings with reduced crosstalk in expense for slight increase in the loss will contribute to the switch fabric scalability. The crosstalk for the TE mode only has been shown to be a lot lower than the considered in this study, hence using this mode only can increase the switch scalability. Other possibility to avoid the detrimental effects of the crossing is to go beyond planar switches with 3D integration for example [57, 58].

As discussed in Section 2.2 significant technological advances have been made in producing low loss, CMOS compatible ring waveguides. As the analysis showed the ring loss is a crucial parameter for the scalability of the microring switch fabric. Very low loss rings of below 0.065 dB/cm have been demonstrated using silicon nitride [59] indicating that far higher-port counts can be achieved.

Link reservation protocols and arbitration schemes must be conceived in accordance to the physical layer delays associated with optical link setup and tear down. In a recent demonstration [49] these physical layer delays were measured on the microsecond-scale which currently limits the use of the switch fabric in a circuit-oriented configuration. Intelligent link reservation and arbitration schemes need to be developed in order to make full use of the nanosecond switching times provided by the silicon photonic switch fabric and realize optical packet switching.

6. Conclusions

High-port count photonic switch fabrics that can be dynamically configured at nanosecond rates are essential for reducing network latency and increasing high-bandwidth connectivity in next generation data centers. Silicon photonics with its CMOS compatibility and dense WDM capabilities is an excellent candidate technology for their realization.

In this article we showed that under the considered current state-of-the-art device geometries and parameters, a high radix 128×128 microring based single chip switching fabric is achievable. We demonstrated this by considering a basic switching element comprised of two microrings. This element was designed with broader resonances and low crosstalk. The scalability of the switch elements were assessed by means of calculating the total power penalty for an optical signal. We proposed a way to set the device parameter such that its crosstalk power penalty is minimized. Furthermore we described how the silicon photonic switching fabric can be controlled, managed and hence fully integrated into an optically interconnected data center system design.

The silicon photonic platform is capable of offering energy efficient, scalable high-radix integrated switching fabrics for data center interconnection networks. In this analysis we considered current state-of-the-art parameters. As silicon photonics is a rapidly developing field the device parameters will be expectedly improved. Our analysis indicates that the scalability of the silicon photonic microring based switching fabric can be substantially increased by employing lower loss rings, low crosstalk junctions, and alternative interconnect topologies.

Acknowledgments

We gratefully acknowledge support for this work by the U.S. Department of Energy (DoE) National Nuclear Security Administration (NNSA) Advanced Simulation and Computing (ASC) program through contract PO1319001 and PO 1426332 with Sandia National Laboratories. Sandia National Laboratories is a multi-program laboratory managed and operated by Sandia Corporation, a wholly owned subsidiary of Lockheed Martin Corporation, for the U.S. Department of Energy's National Nuclear Security Administration under contract DE-AC04-94AL85000. David M. Calhoun acknowledges the support of NSF IGERT (DGE-1069260).